High voltage structural evolution and enhanced Na-ion diffusion in P2-$Na_{2/3}Ni_{1/3-x}Mg_xMn_{2/3}O_2$ ($0 \leq x \leq 0.20$) cathodes from diffraction, electrochemical and ab-initio studies

Nuria Tapia-Ruiz[1,*], Wesley M. Dose[2], Neeraj Sharma[2], Hungru Chen[3], Jennifer Heath[3], James Somerville[1], Urmimala Maitra[1], M. Saiful Islam[3], and Peter G. Bruce[1,*]

[1] Department of Materials and Chemistry, University of Oxford, Parks Road, Oxford OX1 3PH, UK
[2] School of Chemistry, UNSW Australia, Sydney, Australia
[3] Department of Chemistry, University of Bath, Bath, BA2 7AY, UK

INTRODUCTION

Lithium-ion batteries have helped in the worldwide revolution in portable electronics due to their high-energy density. However, there are serious concerns about the cost of lithium due to its scarcity and geographically-concentrated availability. In this context, sodium-ion batteries have emerged as a promising alternative, especially when volumetric and gravimetric energy density requirements are not as stringent, *e.g.* grid storage, thereby addressing the issues related to cost and sources [1,2].

Sodium-ion batteries based on layered oxide compounds with general formula Na_xTMO_2 (TM = transition metal) adopting P2-type and O3-type structures [3] have become strong contenders for application. In these structures P and O refer to the Na coordination, *i.e.* trigonal prismatic or octahedral, respectively, while the numerals designate the repeated transition metal oxide stacking within the unit cell (ABBA and ABCABC for "2" and "3", respectively). Layered P2-type compounds have shown enhanced electrochemical performance as they generally undergo fewer structural transitions when (de)intercalating Na-ions compared to O3 [1]. In particular, P2-$Na_{2/3}Ni_{1/3}Mn_{2/3}O_2$ has shown promise due to its high theoretical capacity (*ca.* 170 mAh g^{-1}) and high average voltage (*ca.* 3.5 V) because of the presence of the active Ni^{2+}/Ni^{4+} redox couple. However, the material possesses poor cycle life, which has been attributed to the gliding of the transition metal layers at high voltages and subsequent formation of the O2 phase [4,5]. In addition, the plateaux occurring upon charge/discharge have been attributed to specific sodium ordering patterns in the edge-shared and face-shared sodium sites when sodium contents are 1/2 and 1/3 [6].

Sodium ordered compounds are thermodynamically more stable than their disordered counterparts, impeding Na^+ mobility, which results in poorer performance at high current rates [6,7]. To date, researchers have made considerable efforts to improve the electrochemical performance of P2-$Na_{2/3}Ni_{1/3}Mn_{2/3}O_2$ by strategic doping of this material with selected cations, namely Li^+, Cu^{2+}, Al^{3+}, Zn^{2+} and Ti^{4+} [8-12]. Mg^{2+} substitution for Ni^{2+} has shown great promise and hence is one of the most studied approaches [12,13], although the non-redox active behaviour of Mg^{2+} in principle causes a penalty on the overall charge stored in the material. However, there is still a need for greater fundamental understanding of the important effects: the structural role of Mg in the Ni^{2+}/Mn^{4+} honeycomb layers

(along the *ab* plane) and *c* axis, and how its presence/absence affects the Na^+-vacancy order/disorder in these materials and the phases obtained at the end of charge. A more complete understanding of this behaviour will allow us to design battery materials with promising electrochemical performance in terms of cyclability and rate capability. In this study, a series of P2-type $Na_{2/3}Ni_{1/3-x}Mg_xMn_{2/3}O_2$ ($0 \leq x \leq 0.20$) materials were prepared by a conventional solid-state method and were structurally characterised using mainly X-ray and neutron diffraction techniques. Cycling data was performed in half-cells vs. Na at room temperature. Ab initio simulation studies were conducted to examine structural and Na-ion diffusion properties on Mg substitution, complementing the experimental insights.

RESULTS AND DISCUSSION

Crystal structure

P2-$Na_{2/3}Ni_{1/3-x}Mg_xMn_{2/3}O_2$ materials (where $0 \leq x \leq 0.20$) were synthesised from their respective oxides *via* solid-state methods. Elemental analysis from inductively coupled plasma (ICP) spectroscopy confirms the compositions are as targeted (Table S1). Particles of 1-10 µm of diameter and hundreds of nanometers of thickness and hexagonal morphologies were observed (Figure S1). Powder X-ray diffraction (PXRD) was used to confirm the purity of the samples (Figure S2). All Bragg reflections from each individual sample could be assigned to a P2-type layered structure with $P6_3/mmc$ (n° 194) space group. The lattice parameters for the P2-$Na_{2/3}Ni_{1/3}Mn_{2/3}O_2$ sample are comparable to those reported in the literature [5]. A broad reflection at d = 4.2 Å (1/3 1/3 0) (not shown here) was observed in the Mg-containing samples, corresponding to long-range in-plane ordering represented by [$(Mg^{2+}/Mn^{4+})O_6$] honeycomb units (in a $\sqrt{3}a \times \sqrt{3}a$ type supercell) [14] (Figure S2). As intuitively expected, this Bragg reflection becomes more significant at high levels of Mg. The Mg^{2+}/Mn^{4+} honeycomb-type ordering occurs due to the large differences in radii and charge (*ca.* Mg^{2+}/Mn^{4+} = 1.38) [7]. By contrast, elucidation of Ni^{2+}/Mn^{4+} ordering, which is analogous to the Mg^{2+}/Mn^{4+} ordering, was easily evidenced using neutron diffraction (ND) due to their different neutron scattering lengths (see experimental section). A comparison between X-ray and neutron data for the P2-$Na_{2/3}Ni_{1/3}Mn_{2/3}O_2$ sample is shown in Figure 1a.

ND data at room temperature for the P2-$Na_{2/3}Ni_{1/3-x}Mg_xMn_{2/3}O_2$ ($0 \leq x \leq 0.20$) series is shown in Figures 1b and 1c. Selected Rietveld refined crystallographic parameters from ND data are presented in the SI. An increase in the lattice parameters was observed upon Mg-replacement due to the slightly larger size of Mg^{2+} (0.72 Å) when compared to Ni^{2+} (0.69 Å) in octahedral coordination). The cell parameters of $Na_{2/3}Ni_{1/3}Mn_{2/3}O_2$ are in good agreement with those from X-ray data and the literature [5]. Data were refined using the Rietveld method using an AB-type crystallographic model ($P6_3$ space group) [15,16]. This structural model considers a larger hexagonal unit cell than that described by the $P6_3/mmc$ space group, with in-plane [$((Ni^{2+}/Mg^{2+})/Mn^{4+})O_6$] honeycomb stacking layers which are not superimposed along the c-axis, hence the A-B nomenclature. This superstructure differs from the AA-type, reported in the $Na_{2/3}Mg_{1/3}Mn_{2/3}O_2$ material by Paulsen et al. [16], where honeycomb ordered layers overlay along the c axis [16]. In the model, we have considered that Ni^{2+} and Mg^{2+} ions are located at the same octahedral 2b sites due to their identical pristine charge and relatively similar sizes, whereas Mn^{4+} atoms

are located in both 2a and 2b sites in the MO_2 layers; larger Na ions are located in between MO_2 layers in trigonal prismatic sites (*i.e.* 6c sites predominantly (*ca.* 75% Na available) as these correspond to the more stable edge sites and in a lower amount in the face-shared 2a and 2b sites). In-plane and inter-plane ordering patterns are characterised by the reflections observed in the $3.4 < d < 4.5$ Å range (Figure 1c) [15]. In-plane Ni(Mg)/Mn long-range ordering is characterised by the 010 and 012 reflections at 4.35 and 3.45 Å respectively, whereas intra-plane Ni(Mg)/Mn long-range ordering is characterised by the 011 reflection at 4.1 Å. These peaks have been indicated in Figure 1c with a (*) sign and are still present in the ND data, even at the largest magnesium content. The AA-type structure differs from the AB-type structure on the absence of the reflection at 4.1 Å [15].

The reflections at d = 3.15 and 3.25 Å are coincident to those observed by Meng et al. [6] when describing the large zig-zag (LZZ)-sodium ordering in prismatic sites on P2-$Na_{2/3}Ni_{1/3}Mn_{2/3}O_2$] (Figure 1c). However, it was not possible to observe in these data the Bragg reflection at *ca.* 3.04 Å reported by Meng et al. [6]. These reflections broaden at the highest Mg content studied here, i.e. x = 0.20 (data shown in pink in Figure 1c). Instead, two extra peaks (marked with a (+) sign) were observed in this sample in the d spacing range studied were also observed in the X-ray data (Figure S2(b)). These peaks were matched to a second phase (*ca.* 20 wt%) that could be refined as a $\sqrt{7}\ a$ x $\sqrt{7}\ a$- type ordered superstructure with hexagonal space group $P6_3/m$ (nº 176), isostructural to $K_4Co_7O_{14}$, and with lattice parameters a = 7.706(3) Å and c = 11.051(6) Å. This structural model was previously used by Imanishi et al. to describe a unique Na ordering in $Na_{0.58}CoO_2$ structure, with Na atoms in two inequivalent Na sites (2b and 6h) which induce a shift of the Co-atom trimers parallel to the c- axis [18].

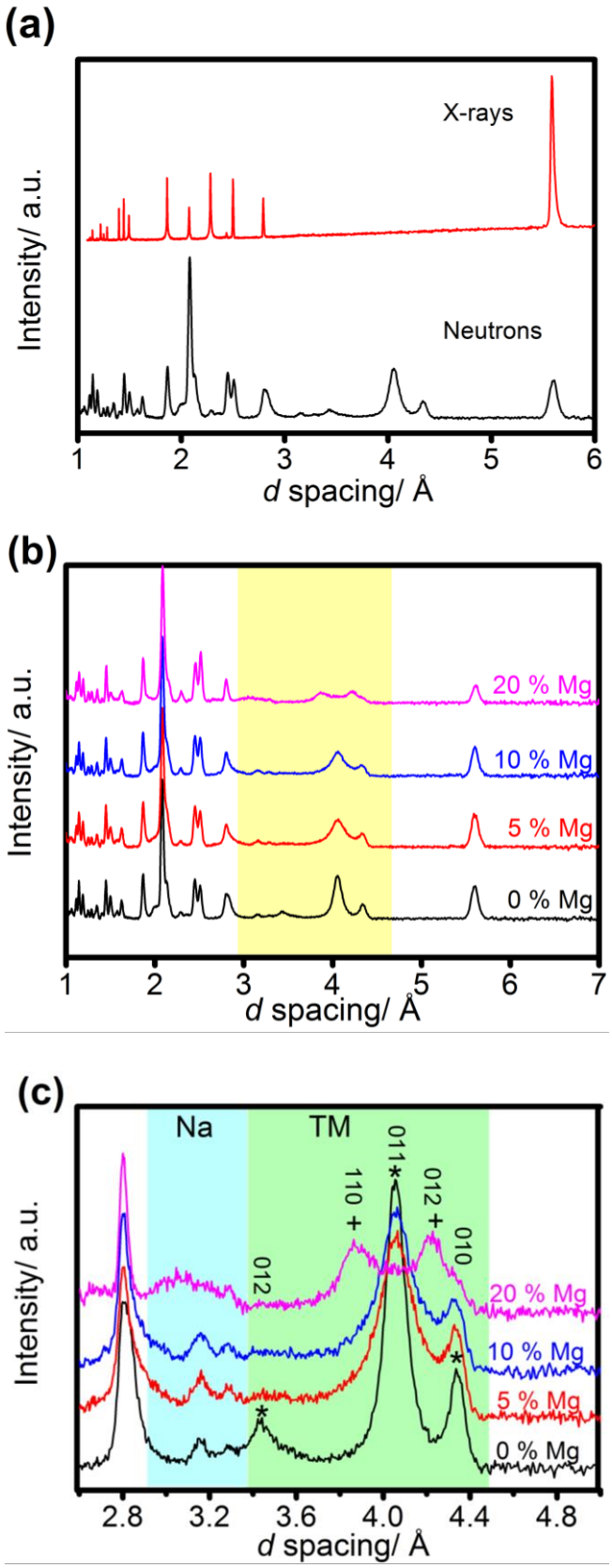

Figure 1. a) X-ray and neutron data comparison for $Na_{2/3}Ni_{1/3-x}Mg_xMn_{2/3}O_2$, where x = 0; b) Stacked plots showing neutron diffraction data for $Na_{2/3}Ni_{1/3-x}Mg_xMn_{2/3}O_2$, where $0 \leq x \leq 0.20$. Yellow-highlighted region represents the d spacing range where ordering features related to sodium and transition metal

atoms have been observed; and c) zoom of the yellow-highlighted region in Figure 1b. Blue-highlighted area shows evolution of peaks related to the zig-zag Na ordered distribution upon Mg concentration. Green-highlighted area shows peaks attributed to inter-plane and intra-plane transition metal ordering. (*) indicates *hkl* reflections indexed using $P6_3$ the space group (nº 173); and (+) indicates *hkl* reflections indexed using the $P6_3/m$ space group (nº 176).

Electrochemical performance in Na-half cells

Charge/discharge galvanostatic curves of the P2-$Na_{2/3}Ni_{1/3-x}Mg_xMn_{2/3}O_2$ ($0 \leq x \leq 0.20$) samples in the voltage range 2-4.5 V are shown in Figure 2a. The experimental capacities obtained in P2-$Na_{2/3}Ni_{1/3}Mn_{2/3}O_2$ are comparable to those reported in the literature [5,6]. Contrary to our calculations where we consider exclusively the electrochemical oxidation of Ni^{2+} (found in the pristine materials using XANES (Figure S7)) to Ni^{4+}, we have observed experimental capacities larger than expected in the magnesium substituted samples. Here, we have assumed that the Mn^{4+} observed by XANES in the pristine materials does not have any electrochemical activity, i.e. does not oxidise to Mn^{5+} as described in other reports from Mn-containing compounds [17]. This behaviour is notably more significant when x = 0.20, where an extra 38 mAh g^{-1} was achieved on the first charge. Similar electrochemical behaviour was reported by Yabuuchi et al. in P2-$Na_{0.67}Mg_{0.28}Mn_{0.72}O_2$ and their explanation for the abnormally high capacity (about 100 extra mAh g^{-1}) was attributed to oxygen participation [14].

The replacement of Ni^{2+} by Mg^{2+} ions favours the initial capacity retention on cycling [12,13], with a higher cycling efficiency when $x \geq 0.10$ (Figure 2b). A slight increase in discharged specific capacities was observed in the first 20 cycles for the $x \geq 0.1$ samples, although this effect is more pronounced in the x = 0.2 sample. In this cycle range, specific capacities increased 4.5 % and 12.6 % for x = 0.1 and x = 0.2 samples, respectively. dQ/dV plots were used to further study the increase in capacity in these samples, which revealed an irreversible high voltage feature occurring at *ca.* 3.9 V upon increased cycling (Figure S8). The enhanced capacity retention in magnesium-substituted samples compared to the P2-$Na_{2/3}Ni_{1/3}Mn_{2/3}O_2$ material has been explained by the switch from the detrimental O2 phase, observed in this material at high voltages, to the intergrowth OP4 phase [13].

Furthermore, smoother charge and discharge curves were observed upon Mg^{2+} substitution (these being optimal when x = 0.2), indicating a predominant solid-solution reaction mechanism. This is clearly indicated in the dQ/dV plots shown in Figure 2c. Single phase reactions on cycling caused by Na^+ vacancy disorder have been related to high Na^+ conductivity and excellent high-rate electrochemical performance [7]. Structural changes upon cycling of these samples were then analysed by *in operando* diffraction methods described in the next section.

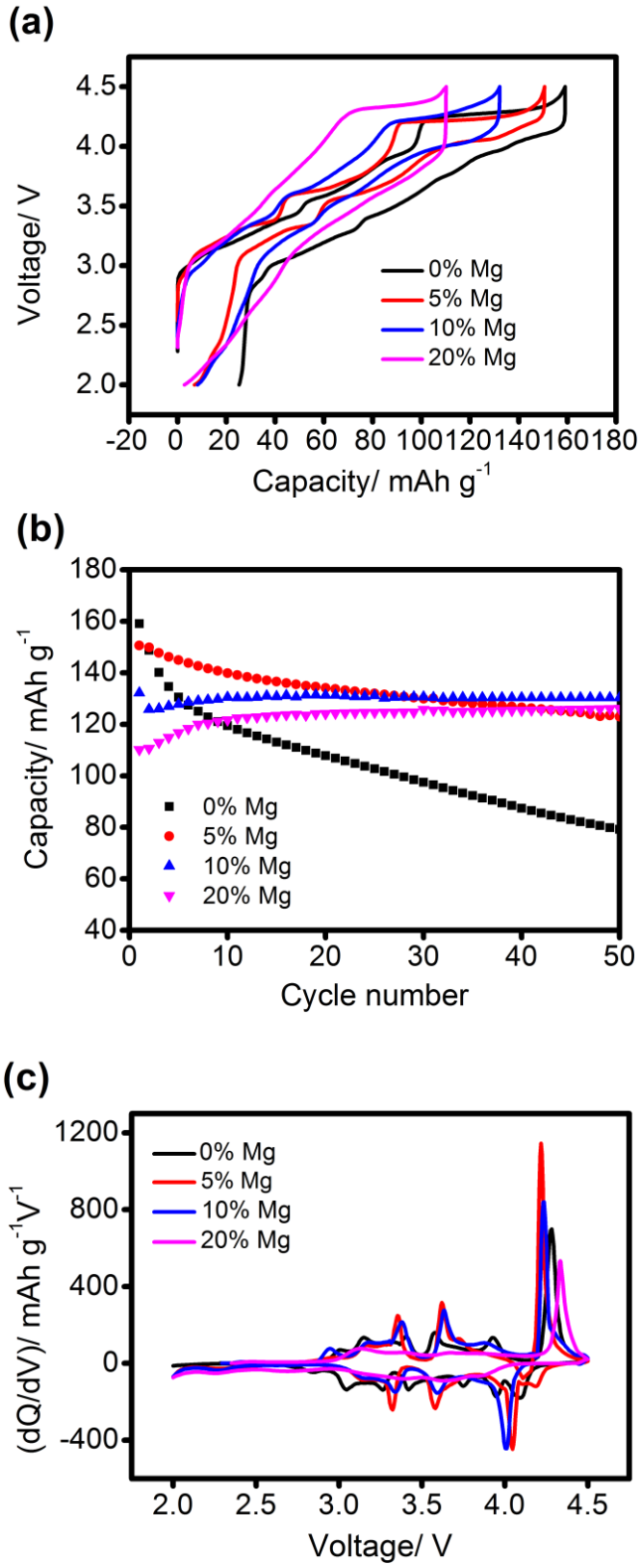

Figure 2. First charge and discharge curves for $Na_{2/3}Ni_{1/3-x}Mg_xMn_{2/3}O_2$, where $0 \leq x \leq 0.20$, in the voltage range 2-4.5 V at 10 mA g^{-1}; b) Discharge cycling data (up to 50 cycles) for samples shown in Figure 1; and c) Differential capacity curves for data shown in Figure 2a.

Structural evolution from *In operando* X-ray diffraction

Structural evolution determined from the *in operando* synchrotron XRD experiments during sodium (de)intercalation in the P2-$Na_{2/3}Ni_{1/3-x}Mg_xMn_{2/3}O_2$ ($0 \leq x \leq 0.20$) series is shown in Figure 3 for the (002) and (100) reflections (space group $P6_3/mmc$). Rietveld analysis of the patterns collected before cycling (Tables S7-S9) were in good agreement with the powder-only structural models. In general, during charge (sodium removal) the 00*l* reflections shift to lower angles, an expansion of the *c* axis; while the *h*00 and *h*0*l* reflections shift to higher angles, a contraction in the *a* axis. The reverse trends were observed during discharge (sodium insertion), in agreement with those reported previously from *ex-situ* data for x = 0 [5,6].

P2-$Na_{2/3}Ni_{1/3}Mn_{2/3}O_2$ evolution

Without Mg substitution (x = 0) the structure undergoes a series of two-phase reactions during overall expansion and contraction below 4.0 V, and above 4.2 V. As reported in earlier work, the phase transformation from P2 to O2 occurs above 4.2 V on charge and is associated with the 4.28 V plateau [5,7]. Increased repulsion between successive O layers (directly facing each other in the P2 structure (ABBA)) at low sodium content prompts the MO_2 sheets to glide in the a-b plane to transform into the O2 structure (ABCB). Total energy calculations have shown this to be the more stable phase after removing all Na ions [6]. Lu and Dahn first proposed that the voltage plateaux at 3.0 and 3.6 V correspond to specific Na ion ordering at x = 1/2 and 1/3 respectively [5]. Meng and co-workers [6] used first principles calculations to model the nature of the ordering and the structure of these intermediate phases.

The high resolution *in operando* synchrotron XRD experiments described in our work provide experimental evidence for the intermediate phases, and demonstrate how these phases evolve with respect to time and potential. Sequential Rietveld refinements were carried out to determine the lattice parameters and weight fraction of the respective phases (Figure 4, and details of the fits are given in the SI). On charge at 50 mA g^{-1} two phases were clearly resolved prior to the P2-O2 phase transition. The new phase appears at 3.5 V, coinciding with the first voltage step, and the lattice parameters of this new phase evolve rapidly (*a* decreased while *c* increased) through to 3.8 V and the second voltage step, after which they stabilised at their minimum and maximum values, respectively. Discharge (sodium insertion) was performed specifically at a slower rate (10 mA g^{-1}) to give better resolution of the phase changes, and thus these are discussed in more detail.

Upon sodium insertion, the P2 and O2 phases coexist from the charged state to the end of the 4.0 V plateau. Three P2 phases were observed thereafter, corresponding to the 3.6, 3.0 and 2.3 V plateaux. The lattice parameters of the three P2 phases (at the maximum phase weight fraction) are compared to the x = 1/3, 1/2 and 2/3 sodium ordered structures reported by Meng and co-workers (*ex-situ* data) [6] in Figure 5. Although Figure 5 compares the dynamic/metastable structure (this work) with the relaxed/equilibrium structure [6], there is a good agreement between these data. Therefore, based on the comparisons of the structures and the approximate composition (derived from the electrochemistry)

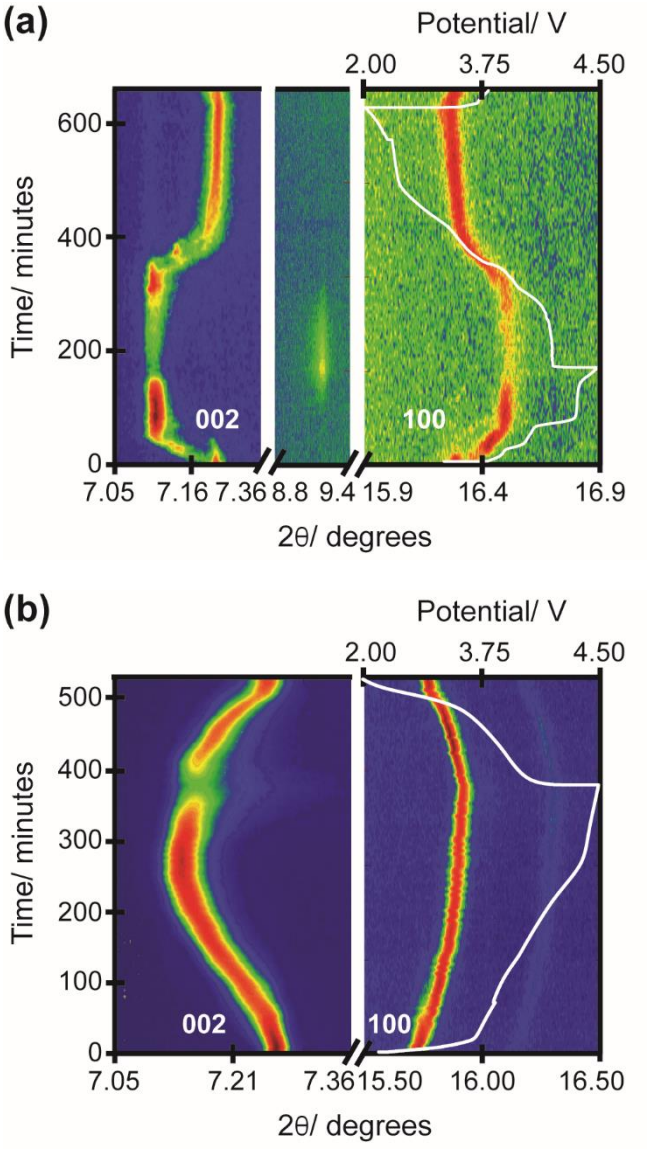

Figure 3. Selected 2θ regions of *in operando* synchrotron XRD data highlighting the evolution of the (002) and (100) reflections for $Na_{2/3}Ni_{1/3-x}Mg_xMn_{2/3}O_2$ where a) x = 0; and b) x = 0.2. The colour scale represents reflection intensity and the potential profiles are included.

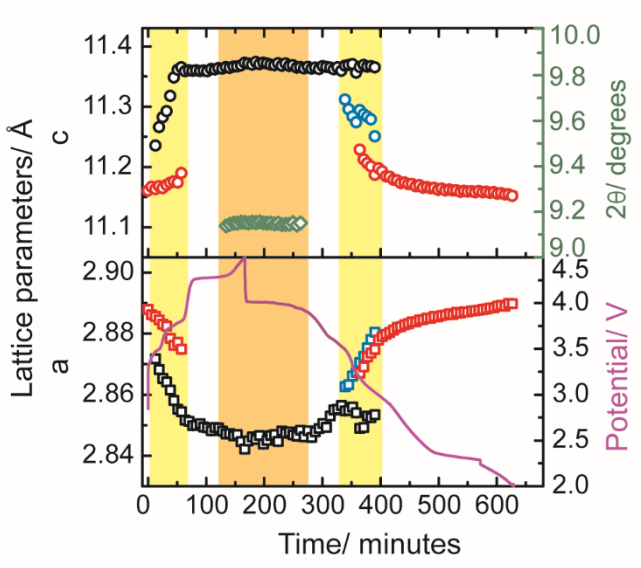

Figure 4. Changes in *a* and *c* lattice parameters of the $Na_{2/3}Ni_{1/3}Mn_{2/3}O_2$ electrode (x = 0) during charge-discharge, together with the electrochemical profile. The lattice parameters of the P2 ordered phases are shown in black (1/3 Na), blue (1/2 Na) and red (2/3 Na), and the 2θ position of the 002 reflection from the O2 phase is shown in green. Error bars are within the symbols. The two yellow shaded regions indicate the phase transitions between P2 sodium ordered structures and the orange shaded region indicates the P2 to O2 phase transition.

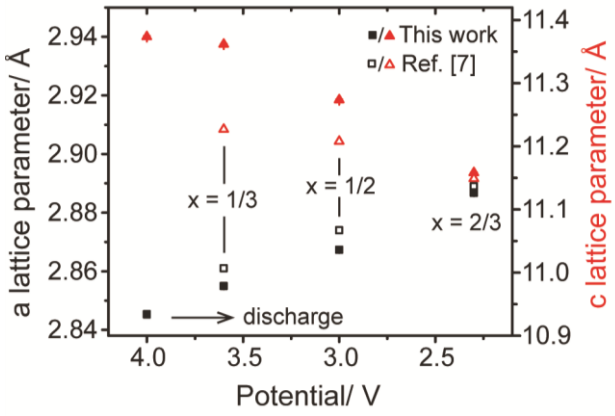

Figure 5. Comparison of the lattice parameters at the 4.0 V, 3.6 V, 3.0 V and 2.3 V plateaux on discharge collected *in operando* in this work (filled data) with the lattice parameters of the x = 1/3, 1/2 and 2/3 ordered structures (4.0 V, 3.5 V and before charging respectively) collected *ex-situ* during charge by Meng and co-workers (open data) [6]. Error bars are included within the symbols.

it can be concluded that the intermediate phases observed in our *in operando* work agree with the proposed compositions in the literature. This is the first time that experimental evidence for the Na ion ordered structures are reported and discussed in $Na_{2/3}Ni_{1/3-x}Mn_{2/3}Mg_xO_2$, confirming the calculated structures reported previously [6].

Effect of Mg substitution above 4 V

From a visual inspection of the *in operando* synchrotron XRD pattern evolution (Figure 3) and the electrochemical profiles (Figure 2a) it is clear that Mg-substitution has had a significant effect on the phase evolution. Adding 10 % Mg (x = 0.1) was sufficient to supress the P2 to O2 phase transition, in agreement with Wang *et al.* [19]. However, upon sodium removal above 4.3 V we observed a loss of reflection intensity and a broad reflection at 2θ = 7.35° (Figure S9), which is not discussed in ref. [19]. This phase transition we identify as the P2 to OP4 transition, where the OP4 phase shows alternate stacking of octahedral and trigonal prismatic sodium layers along the c axis, as has been previously identified in $Na_{2/3}Fe_{1-y}Mn_yO_2$ materials [20]. While substitution of 20 % Mg did not prevent the P2 reflections losing intensity in the charged state, the OP4 reflection was no longer observed in the first charged state (Figure 6). However, asymmetric broadening of the (002) reflection indicated the presence of stacking faults.

DFT calculations have also shown the inhibition of P2 to O2 phase transformation. Without Mg, all Na^+ ions can theoretically be extracted from the structure of $Na_{2/3}Ni_{1/3}Mn_{2/3}O_2$ at the end of the charge, accompanied by the oxidation of Ni^{2+} to Ni^{4+}. Empty Na layers then enables the gliding of MO_2 sheets and results in the transformation from P2 to O2 structures [5,6,21]. In the Mg substituted $Na_{2/3}Ni_{1/3-x}Mg_xMn_{2/3}O_2$ samples, two Na^+ ions must stay in the vicinity of a Mg^{2+} ion at high voltages (*ca.* 4.2 V), in order to keep the local charge neutrality. This prevents the formation of consecutive empty Na layers and hence the transformation to the O2 structure is inhibited. Figure 7 shows two possible local structures around the Mg^{2+} ion during the P2-OP4 phase transformation. The first situation, (a), is where both Na^+ ions are located on the same side of the MO_2 sheet and therefore one Na layer is completely empty. The empty layer then enables gliding of MO_2 sheets resulting in O type stacking. The second situation, (b), is where the two Na^+ ions are located on each side of the MO_2 sheet. Our DFT calculations have examined these structures and indicate that the first configuration is more energetically stable, which is consistent with the experimentally observed P2 to OP4 transition in the Mg substituted samples, especially for x = 0.1.

Effect of Mg substitution below 4 V

Mg doping smoothed the charge/discharge profile below 4 V [19]. Comparison of the *in operando* XRD patterns revealed that at x = 0.1 this was caused by subtler P2 to $P2_{new}$ phase changes (both showing similar lattice parameters) (SI). These are more distinct at faster cycling rates, with clearer two-phase behaviour observed during charge at 100 mA g^{-1} than discharge at 8.5 mA g^{-1}. By increasing the Mg fraction to x = 0.2, however, the two-phase behaviour is replaced by continuous reflection evolution characteristic of a solid solution reaction. This correlates with the electrochemical observations of

smoother charge/discharge curves and illustrates the “removal” of the ordered structures during charge/discharge. These more gradual structural changes upon Na (de)intercalation have also been observed in P2 $Na_{2/3}Mn_{1-y}Mg_yO_2$ [22], where *ex situ* ^{23}Na solid state MAS NMR was used to demonstrate that Mg doping leads to more continuous changes in the Na resonances and to fewer, sharper peaks during the first cycle. The absence of ordered structures or the insertion/extraction reactions via disordered states, especially in terms of Na^+-vacancy disorder, have been related to high Na^+ conductivity and excellent high-rate performance [7]. Our work provides direct evidence for the variation in structural order as a function of Mg concentration with respect to electrochemical processes.

Effect of Mg substitution on volume change

As discussed above, Mg substitution gave rise to an overall increase in the unit cell volume. In turn, this results in reduced volume contraction/expansion on sodium extraction/insertion. At x = 0.1 and 0.2, the unit cell contraction of the P2 phase on first charge is over half that of the x = 0 material (% vol. contraction of 0.56 % and 0.52 %, respectively, compared to 1.30 % for x = 0). The subsequent % vol. expansion of the x = 0.2 material (0.11 %) is also considerably less than either the x = 0 (0.93 %) or x = 0.1 (0.58 %) samples. The trend in the volume change with Mg content agrees well with the electrochemical performance effect, where increased Mg levels improve performance.

In operando synchrotron XRD data have conclusively revealed that during charge-discharge below 4 V the Na ion ordered intermediates are removed as the Mg concentration increases, which in turn leads to smoother charge/discharge profiles and better electrochemical performance. Additionally, the x = 0.1 sample suppresses the formation of the O2 phase, transitioning instead to the intermediate OP4 structure, while higher Mg concentrations of x = 0.2 appear to minimise the transition to the OP4. This correlates with the dramatic reduction in the volume change during charge/discharge as the Mg concentration is increased. All these structural factors point towards superior electrochemical performance of the Mg-substituted samples.

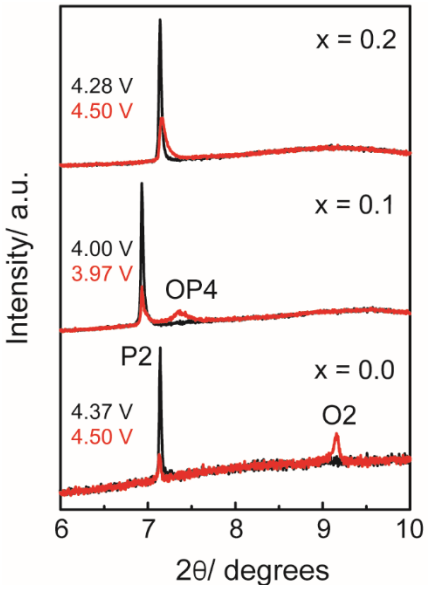

Figure 6. *In operando* XRD patterns for $Na_{2/3}Ni_{1/3-x}Mg_xMn_{2/3}O_2$, where $0 \leq x \leq 0.20$, prior to the charged state (black) and in the charged state (red) between 6° and 10° 2θ. The red XRD pattern shown for x = 0.1 is 10 minutes after the charged state (3.97 V) where the OP4 reflection is most intense.

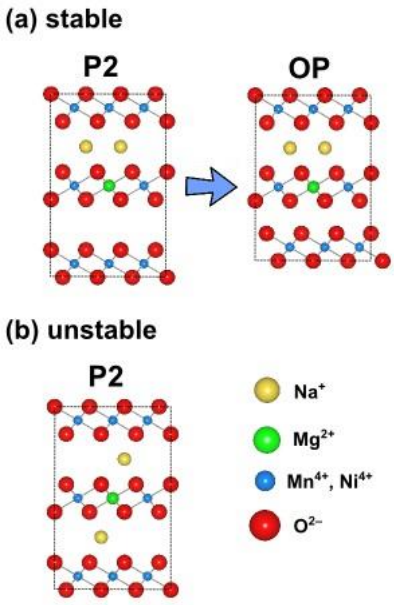

Figure 7. Two possible local structures around the Mg^{2+} ion at 4.2 V. (a) The low energy configuration, where two Na ions are located at the same side of the MO_2 sheet and the empty Na layer allows the transformation from P stacking to O stacking. (b) The high energy configuration, where two Na ions are located on each side of the MO_2 sheet.

Effect of Mg substitution on Na^+ diffusion

Na-ion diffusion in P-type layered oxide compounds has been shown to be faster than in O-type compounds [23,24]. Strong in-plane Na-Na interactions makes Na-ion diffusion highly correlated [23]. It is therefore necessary to perform molecular dynamics simulations to probe such diffusion mechanisms and to complement the experimental measurements. The simulated Na diffusion in $Na_{0.56}Ni_{0.33}Mn_{0.67}O_2$ and $Na_{0.56}Mg_{0.11}Ni_{0.22}Mn_{0.67}O_2$ from ab initio molecular dynamics (AIMD) simulations are shown as mean square displacements in Figure 8. In agreement with the galvanostatic intermittent titration technique (GITT) and nuclear magnetic resonance (NMR) measurements on this family of compounds [13], our simulations suggest that Mg substitution leads to an increase in Na-ion diffusivity. Na diffusion coefficients (D_{Na}) derived from classical MD also predict this increase of Na diffusion with Mg replacement; values of 2.5 x 10^{-9} cm^2 s^{-1} and 1.2 x 10^{-8} cm^2 s^{-1} (at 300 K) are obtained for $Na_{0.56}Ni_{0.33}Mn_{0.67}O_2$ and $Na_{0.56}Mg_{0.11}Ni_{0.22}Mn_{0.67}O_2$ respectively. The enhancement in Na diffusion has been attributed to the enlargement of interlayer spacing upon Mg doping [25]. However, the estimated change in interlayer separation is very small (less than 0.05 Å).

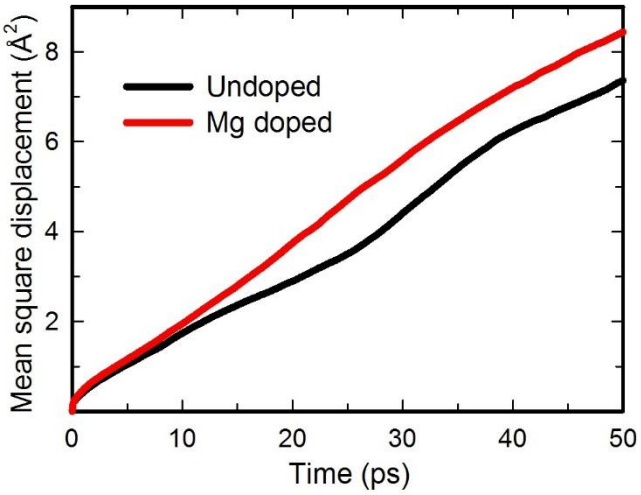

Figure 8. Mean square displacements of Na ions in $Na_{0.56}Ni_{0.33}Mn_{0.67}O_2$ and $Na_{0.56}Mg_{0.11}Ni_{0.22}Mn_{0.67}O_2$ from ab initio molecular dynamics (AIMD) simulations, indicating faster Na-ion diffusion in the Mg-containing compound.

Electrochemical data of $Na_{2/3}Ni_{1/3}Mn_{2/3}O_2$ have shown sodium ordering and phase separation (Figure 2a), which results in rich structural and electronic phase diagrams [26-29]. The electrochemically inactive Mg^{2+} (with fixed 2+ charge) and its random distribution over Ni sites can effectively suppress the development of long-range charge ordering within the MO_2 sheet and hence inhibit long-range sodium ordering (see x = 0.2 experimental case detailed above). As a result, charge and discharge would proceed through a more solid-solution like reaction with a higher Na-ion diffusivity, as reflected in a more sloping charge-discharge profile (Figures 2a and 3c). Furthermore, our AIMD simulations on $Na_{0.56}Mg_{0.11}Ni_{0.22}Mn_{0.67}O_2$, show that the Mg ion displaces in the z direction with a larger amplitude than both Ni and Mn, as shown in Figure 9. This can be attributed to the ionic nature of the Mg-O bond and hence less rigid MgO_6 octahedra. In contrast, the relatively higher degree of covalency in Ni-O and Mn-

O bonds, owing to strong 3d-2p hybridization [30,31], makes the NiO_6 and MnO_6 octahedra more rigid. The large displacement of Mg^{2+} in the z direction consequently alters the electrostatic potential felt by Na^+ ions and has a beneficial effect on Na diffusion. An interesting comparison includes a previous NMR study indicating that Li^+ ions (which have a very similar ionic radius to Mg^{2+}) were displaced from transition metal layers to the Na layers in the P2-$Na_x[Li_yNi_zMn_{1-y-z}]O_2$ material [21].

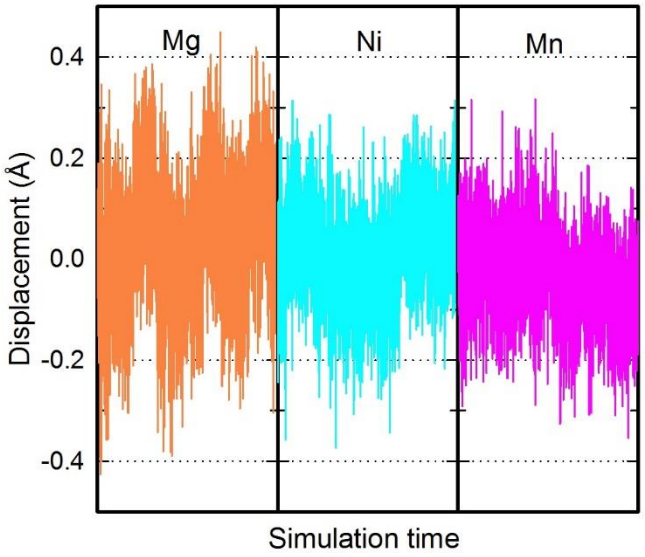

Figure 9. Displacement of Mg, Ni and Mn ions in the z-direction in $Na_{0.56}Mg_{0.11}Ni_{0.22}Mn_{0.67}O_2$ during the 50 ps AIMD simulation, indicating larger amplitudes for Mg.

CONCLUSIONS

In this work we have demonstrated the effects of Mg substitution on the structure of a series of P2-$Na_{2/3}Ni_{1/3-x}Mg_xMn_{2/3}O_2$ compounds. Combined XRD and neutron analysis show that magnesium substitutes nickel in the Ni-Mn honeycomb layers, forming an AB-type structure as in the parent material. Hence there is no structural re-arrangement in the c-axis upon Mg substitution. We have also shown that high levels of Mg in the structure (*i.e.* x = 0.2) lead to a more disordered distribution of sodium in the pristine material. Electrochemical results corroborate our structural data by showing a solid-solution profile. Importantly, this is the highest level of Mg substitution in the P2-$Na_{2/3}Ni_{1/3-x}Mn_{2/3}O_2$ compound reported to date. The high resolution *in operando* synchrotron XRD experiments provide evidence for the x = 1/2 and x = 1/3 intermediate Na^+-vacancy ordered phases in P2-$Na_{2/3}Ni_{1/3}Mn_{2/3}O_2$. Furthermore, we have shown that Mg substitution effectively disrupts the Na^+-vacancy ordering leading to more gradual structural changes, and suppresses the P2-O2 transition at high voltages, switching it to an OP4 phase. Ab initio molecular dynamics studies have indicated that Na-ion diffusivity increases and that the OP4 phase is the most thermodynamically stable phase at high voltages in the Mg-substituted compounds.

The results of this work have shed new light on the role of magnesium in the high-voltage P2-$Na_{2/3}Ni_{1/3}Mn_{2/3}O_2$ cathode. Understanding the structural and electrochemical changes occurring in cathode materials when a dopant is added to the system is of paramount importance in the design of novel materials with enhanced electrochemical performance.

METHODS

Synthesis

Samples were synthesised by ball milling a mixture of Na_2CO_3 anhydrous (Fisher Chemicals), NiO (Sigma Aldrich, nanopowder, < 50 nm particle size), MnO_2 (Sigma Aldrich, -325 mesh, 99%) and MgO (Sigma Aldrich, -325 mesh, $\geq$ 99% trace metal basis) in acetone in stoichiometric ratios in a Planetary Ball Mill PM 100 (Retsch) for 1 h at 450 rpm using a 2:1 ball-to-powder-ratio. The mixture was left to dry in air and the powders were pressed as pellets under a load of 4 tons cm^{-2} before calcining at 800-850 °C for 12 h in air followed by slow cooling in the furnace. Samples were kept in an Ar filled glove box maintained at < 0.1 ppm H_2O and O_2.

Characterisation

Powder X-ray diffraction (PXRD) patterns were recorded on a 9 KW Rigaku Smartlab diffractometer using Cu $K\alpha_1$ radiation (λ = 1.54051 Å). A customized air-tight sample holder covered with Kapton film was used to avoid severe air/moisture contact during measurement.

Chemical analyses were performed by Inductively Coupled Plasma (ICP) using a Perkin Elmer Elan 6100 DRC ICP-MS.

Time-of-flight powder neutron diffraction data were collected on the GEM high-intensity, medium-resolution instrument at ISIS, Rutherford Appleton Laboratories. Neutron scattering lengths of 0.363, 1.03, 0.566, -0.373 and 0.5803 (all × 10^{-12} cm) were assigned to Na, Ni, Mg, Mn, and O, respectively [32].

Mn and Ni K-edge X-ray absorption near edge structure (XANES) measurements of the pristine materials were performed at the B18 beamline at the Diamond Light Source, UK. The XANES spectra were collected in transmission mode and the intensities of both the incident and transmitted X-ray beams were measured using gas-filled ionisation chambers. Mn and Ni foil were placed in front of a third ionisation chamber and were used to correct any drift in the monochromator. Three scans were performed for each sample. Athena software was used to sum the scans, calibrate and normalise the data and extract the background. Mn_2O_3, MnO_2, NiO and K_2NiF_6 were used as references for Mn^{3+}, Mn^{4+}, Ni^{2+} and Ni^{4+}, respectively.

Electrodes were prepared by mixing the active material with Super S carbon and a 5 wt% solution of PVDF (Polyvinylidene fluoride) in NMP (N-Methyl-2-pyrrolidone) in a 75:15:10 weight ratio. Slurries of the mixtures were prepared by adding *ca.* 1 ml of NMP to the mixture under constant stirring for 3-4 h. The slurry was cast onto Al foil that acts as current collector in an argon-filled glovebox. Loading of

active material for the galvanostatic cycling is 2-3 mg cm^{-2}. The coated foil was dried under vacuum at 80 ° C for 2 h and electrodes of 20 mm were punched out and pressed under a load of 4 tons cm^{-2}.

Galvanostatic charging/discharging tests were performed in CR2325 coin cells using 1 M $NaPF_6$ (99.99% Sigma Aldrich) in PC (propylene carbonate) as the electrolyte solution and sodium metal as the counter electrode. Coin cells were charged/discharged at 10 mA g^{-1} in the 2-4.5 V range.

In operando X-ray diffraction

Customised half cells with 3 mm diameter holes in the casing and 5 mm diameter holes in the stainless spacer were used for the construction of the coin cells for the *in operando* measurements. The coin cells contained the electrodes described above, Na metal (~ 1 mm thickness), a glass fibre separator and 1 M $NaPF_6$ in PC (propylene carbonate) electrolyte solution. *In operando* synchrotron XRD experiments were performed within 1-2 days after cell construction. Data were collected on the Powder Diffraction beamline [33] at the Australian Synchrotron with a wavelength (λ) of 0.70772(2) Å for 0% and 10% and 0.70793(2) Å for 20%, where the wavelength is determined by refining a structural model with data collected on a NIST 660b LaB_6 standard reference material. XRD data were collected continuously in transmission geometry every 4.4(1) minutes for the 10% and 20% samples and 6.4 minutes for the 0% sample. In conjunction, the *in operando* cells were first charged to 4.5 V at relatively fast rates between 30-100 mA g^{-1} and then subsequently discharged to 2 V and charged to 4.5 V at lower rates between 10-30 mA g^{-1}. The electrode loading varied from 1-4 mg cm^{-2} and the current rates were adjusted to accommodate this variation. PXRD and ND data were refined by the Rietveld method using the GSAS software suite with the EXPGUI software interface [34].

Ab initio simulations

Density functional theory (DFT) calculations were performed using the Vienna *ab initio* simulation package (VASP) [35]. Valence electrons were described by a planewave basis set with a cut-off energy of 450 eV. The interactions between valence and core electrons were treated using the projector augmented-wave (PAW) method [36]. The k-space was sampled with k-point mesh spacing smaller than 0.05 $Å^{-1}$. Spin-polarization was enabled and ferromagnetic coupling between magnetic manganese cations was assumed. Structural optimization was performed until the residue force on each atom is smaller than 0.03 eV/Å. Similar DFT methods have been applied successfully to a range of battery materials [37-40]. *Ab initio* molecular dynamics (AIMD) simulations were carried out to study Na^+ ion diffusion in $Na_{0.56}Ni_{0.33}Mn_{0.67}O_2$ and $Na_{0.56}Mg_{0.11}Ni_{0.22}Mn_{0.67}O_2$ with supercells containing 192 atoms. Each composition was first equilibrated for 10 picoseconds. Statistical properties were then obtained by the following 50 picoseconds simulations using the NVT ensemble with a Nosé-Hoover thermostat [41, 42]. All molecular dynamics simulations were performed at 500 K with a time step of 2 femtoseconds. Gamma-point only was used in the k-space sampling in order to keep the computational cost affordable.

CONFLICTS OF INTEREST

There are conflicts to declare.

ACKNOWLEDGEMENTS

P.G.B and M.S.I are grateful to the Engineering and Physical Sciences Research Council (EPSRC) including the SUPERGEN Energy Storage Hub for financial support (EP/L019469/1). We additionally thank the Australian Research Council, (grants DE160100237 and DP170100269) for financial support and the HPC Materials Chemistry Consortium (EP/L000202/1) for Archer supercomputer facilities. Neutron diffraction experiments were performed at the GEM beamline at the ISIS spallation source at the Rutherford Appleton Laboratory, UK. We would like to thank Dr. Robert Armstrong for helpful discussions on neutron data refinements. XANES measurements were performed at the B18 beamline of Diamond Light Source, UK. The authors are grateful to G. Cibin and S. Ramos for contributing to XAS data collection. A component of this research was undertaken on the Powder Diffraction beamline at the Australian Synchrotron, part of the Australian Nuclear Science and Technology Organisation (ANSTO). We would like to thank James C. Pramudita for assistance with cell preparation for the synchrotron studies.

REFERENCES

1. Han, M. H.; Gonzalo, E; Singh, G.; Rojo, T. A comprehensive review of sodium layered oxides: powerful cathodes for Na-ion batteries. *Energy Environ. Sci.* **2015**, 8, 81-102.

2. Ortiz-Vitoriano, N; Drewett, N. E.; Gonzalo, E.; Rojo, T. High performance manganese-based layered oxide cathodes: overcoming the challenges of sodium ion batteries. *Energy Environ. Sci.* **2017**, 10, 1051-1074.

3. Delmas, C.; Fouassier, C.; Hagenmuller, P. Structural classification and properties of the layered oxides. *Phys. B+C* **1980**, 99, 81–85.

4. Lu, Z.; Dahn, J. R. Can all the lithium be removed from T2-$Li_{2/3}[Ni_{1/3}Mn_{2/3}]O_2$? *J. Electrochem. Soc.* **2001**, 148, A710–A715.

5. Lu, Z.; Dahn, J. R. In-situ X-ray diffraction study of P2-$Na_{2/3}[Ni_{1/3}Mn_{2/3}]O_2$. *J. Electrochem. Soc.* **2001**, 148, A1225–A1229.

6. Lee, D. H.; Xu, J.; Meng, Y. S. An advanced cathode for Na-ion batteries with high rate and excellent structural stability. *Phys. Chem. Chem. Phys.* **2013**, 15, 3304–3312.

7. Wang, Y.; Xiao, R.; Hu, Y.-S.; Avdeev, M.; Chen, L. P2-$Na_{0.6}[Cr_{0.6}Ti_{0.4}]O_2$ cation-disordered electrode for high-rate symmetric rechargeable sodium-ion batteries. *Nature Comm.* **2015**, 6, 1–9.

8. Wu, X.; Xu, G.-L.; Zhong, G.; Gong, Z.; McDonald, J.; Zheng, S.; Fu, R.; Chen, Z.; Amine, K.; Yang, Y. Insights into the effects of zinc doping on structural phase transition of P2-type sodium nickel manganese oxide cathodes for high-energy sodium ion batteries. *ACS Appl. Mater. Interfaces* **2016**, 8, 22227–22237.

9. Yoshida, H.; Yabuuchi, N.; Kubota, K.; Ikeuchi, I.; Garsuch, A.; Schulz-Dobrickb, M.; Komaba, S. P2-type $Na_{2/3}Ni_{1/3}Mn_{2/3-x}Ti_xO_2$ as a new positive electrode for higher energy Na-ion batteries. *Chem. Comm*. **2014**, 50, 3677–3680.

10. Wu, X.; Guo, J.; Wang, D.; Zhong, G.; McDonald, M. J.; Yang, Y. P2-type $Na_{0.66}Ni_{0.33-x}Zn_xMn_{0.67}O_2$ as new high-voltage cathode materials for sodium-ion batteries. *J. Power Sources* **2015**, 281, 18–26.

11. Wang, L; Sun, Y.-G.; Hu, L.-L.; Piao, J.-Y.; Guo, J.; Manthiram, A.; Ma, J.; Cao, A.-M. Copper-substituted $Na_{0.67}Ni_{0.3-x}Cu_xMn_{0.7}O_2$ cathode materials for sodium-ion batteries with suppressed P2-O2 phase transition. J. Mater Chem. A **2017,** 5, 8752-8761.

12. Zhao, W.; Kirie, H.; Tanaka, A.; Unnoa, M.; Yamamoto, S.; Noguchi, H. Synthesis of metal ion substituted P2-$Na_{2/3}Ni_{1/3}Mn_{2/3}O_2$ cathode material with enhanced performance for Na ion batteries. *Mater. Lett.* **2014**, 135, 131–134.

13. Singh, G.; Tapia-Ruiz, N.; Lopez del Amo, J. M.; Maitra, U.; Somerville, J. W.; Armstrong, A. R.; Martinez de Ilarduya, J.; Rojo, T.; Bruce, P. G. High Voltage Mg-Doped $Na_{0.67}Ni_{0.3-x}Mg_xMn_{0.7}O_2$ (x = 0.05, 0.1) Na-Ion Cathodes with Enhanced Stability and Rate Capability. *Chem. Mater.* **2016**, 28, 5087–5094.

14. Yabuuchi, N.; Hara, R.; Kubota, K.; Paulsen, J.; Kumakura, S.; Komaba, S. New electrode material for rechargeable sodium batteries: P2-type $Na_{2/3}[Mg_{0.28}Mn_{0.72}]O_2$ with anomalously high reversible capacity. *J. Mater. Chem. A* **2014**, 2, 16851–16855.

15. Yabuuchi, N.; Hara, R.; Kajiyama, M.; Kubota, K.; Ishigaki, T.; Hoshikawa, A.; Komaba, S. New O2/P2-type Li-excess layered manganese oxides as promising multi-functional electrode materials for rechargeable Li/Na batteries. *Adv. Energy Mater.* **2014**, 1301453.

16. Paulsen, J M.; Donaberger, R. A.; Dahn, J. Layered T2-, O6-, O2-, and P2-type $A_{2/3}[M'^{2+}_{1/3}M^{4+}_{2/3}]O_2$ bronzes, A = Li, Na; M´= Ni, Mg; M= Mn, Ti, *Chem. Mater.* **2000**, 12, 2257-2267

17. Freire, M.; Kosova, N. V.; Jordy, C.; Chateigner, D.; Lebedev, O. I.; Maignan, A.; Pralong V. A new active Li–Mn–O compound for high energy density Li-ion batteries, *Nature Mater.* **2016**, 15, 173.

18. Igarashi, D.; Miyazaki, Y. Kajitani, T. Disorder-order transitions in Na_xCoO_2 (x ~0.58), Phys. Rev. B **2008**, 78, 184112.

19. Wang, P.-F.; You, Y.; Yin, Y.-X.; Wang, Y.-S.; Wan, L.-J.; Gu, L.; Guo, Y.-G. Suppressing the P2-O2 phase transition of $Na_{0.67}Mn_{0.67}Ni_{0.33}O_2$ by magnesium substitution for improved sodium-ion batteries. *Angew. Chem. Int. Ed.* **2016**, 55, 7445–7449.

20. Yabuuchi, N.; Kajiyama, M.; Iwatate, J.; Nishikawa, H.; Hitomi, S.; Okuyama, R.; Usui, R.; Yamada, Y.; Komaba, S. P2-type Na(x)[Fe(1/2)Mn(1/2)]O2 made from earth abundant elements for rechargeable Na batteries. *Nat. Mater.* **2012**, 11, 512–517.

21. Xu, J.; Lee, D. H.; Clément, R. J.; Yu, X.; Leskes, M.; Pell, A. J.; Pintacuda, G.; Yang, X.-Q.; Grey, C. P.; Meng, Y. S. Identifying the Critical Role of Li Substitution in P2–$Na_x[Li_yNi_zMn_{1-y-z}]O_2$ ($0 < x, y, z < 1$) Intercalation Cathode Materials for High-Energy Na-Ion Batteries. *Chem. Mater.* **2014**, 26, 1260–1269.

22. Clément, R. J.; Billaud, J.; Armstrong, A. R.; Singh, G.; Rojo, T.; Bruce, P.G.; Grey, C. P. Structurally stable Mg-doped P2-Na2/3Mn1-yMgO2 sodium-ion battery cathodes with high rate performance: insights from electrochemical, NMR and diffraction studies. *Energy and Environ. Sci.* **2016**, 9, 3240-3251.

23. Mo, Y.; Ong, S. P.; Ceder, G. Insights into Diffusion Mechanisms in P2 Layered Oxide Materials by First-Principles Calculations. *Chem. Mater.* **2014**, 26, 5208–5214.

24. Katcho, N. A.; Carrasco, J.; Saurel, D.; Gonzalo, E.; Han, M.; Aguesse, F.; Rojo, T. Origins of Bistability and Na Ion Mobility Difference in P2- and O3-$Na_{2/3}Fe_{2/3}Mn_{1/3}O_2$ Cathode Polymorphs. *Adv. Energy Mater.* **2016**, 7, 1601477.

25. Li, Z-Y.; Gao, R.; Zhang, J.; Zhang, X.; Hu, Z.; Liu, X. New insights into designing high-rate performance cathode materials for sodium ion batteries by enlarging the slab-spacing of the Na-ion diffusion layer. *J. Mater. Chem. A* **2016**, 4, 3453–3461.

26. Roger, M.; Morris, D. J. P.; Tennant, D. A.; Gutmann, M. J.; Goff, J. P.; Hoffman, J. -U.; Feyerherm, R.; Dudzik, E.; Prabhakaran, D.; Boothroyd, A. T.; Shannon, N.; Lake, B.; Deen, P. P. Patterning of sodium ions and the control of electrons in sodium cobaltate. *Nature* **2006**, 445, 631–634.

27. Julien, M.-H.; de Vaulx, C.; Mayaffre, H.; Berthier, C.; Horvatić, M.; Simonet, V.; Wooldridge, J.; Balakrishnan, G.; Lees, M. R.; Chen, D. P.; Lin, C. T.; Lejay, P. Electronic Texture of the Thermoelectric Oxide $Na_{0.75}CoO_2$. *Phys. Rev. Lett.* **2008**, 100, 096405.

28. Lang, G.; Bobroff, J.; Alloul, H.; Collin, G.; Blanchard, N. Spin correlations and cobalt charge states: Phase diagram of sodium cobaltates. *Phys. Rev. B* **2008**, 78, 155116.

29. Ning, F. L.; Golin, S. M.; Ahilan, K.; Imai, T.; Shu, G. T.; Chou, F. C. ^{59}Co NMR Evidence for Charge Ordering below TCO ~ 51 K in $Na_{0.5}CoO_2$. *Phys. Rev. Lett.* **2008**, 100, 086405.

30. de Groot, F. M. F.; Grioni, M.; Fuggle, J. C.; Ghijsen, J.; Sawatzky, G. A.; Petersen, P. Oxygen 1s x-ray-absorption edges of transition-metal oxides. *Phys. Rev. B* **1989**, 40, 5715.

31. Cox, P. A. Transition Metal Oxides: An Introduction to Their Electronic and Properties. *Oxford University Press* **1992**.

32. Sears, V. F. Neutron scattering lengths and cross sections, *Neutron News*, **1992**, 3, 26.

33. Wallwork, K. S.; Kennedy, B. J.; Wang, D. The high resolution powder diffraction beamline for the Australian Synchrotron. *AIP Conf. Proc.* **2006**, 879.

34. Larson A. C.; Von Dreele, R. B. in Los Alamos National Laboratory Report LAUR 86-748, **1994**; Toby, B. H. J. *Appl. Cryst.* **2001**, 34, 210–213.

35. Kresse, G.; Furthmüller, J. Efficient iterative schemes for *ab initio* total-energy calculations using a plane-wave basis set. *Phys. Rev. B* **1996**, 54, 11169–11186.

36. Blöchl, P. E. Projector augmented-wave method. *Phys. Rev. B* **1994**, 50, 17953–17979.

37. Islam M. S. and Fisher C. A. J., Lithium and sodium battery cathode materials: computational insights into voltage, diffusion and nanostructural properties, *Chem. Soc. Rev.* **2014,** 43, 185-204.

38. Armstrong A. R., Lyness C., Panchmatia P., Islam M. S. and Bruce P. G., The lithium intercalation process in the low voltage lithium battery anode $Li_{1+x}V_{1-x}O2$, *Nature. Mater*. **2011,** 10, 223.

39. Chen H., and Islam M. S., Lithium Extraction Mechanism in Li-Rich Li_2MnO_3 Involving Oxygen Hole Formation and Dimerization, *Chem. Mater*., **2016**, 28, 6656.

40. S. P. Ong, V. L. Chevrier, G. Hautier, A. Jain, C. Moore, S. Kim, X. Ma and G. Ceder, *Energy Environ. Sci.* **2011**, 4, 3680.

41. Nosé, S. A unified formulation of the constant temperature molecular dynamics methods. *J. Chem. Phys.* **1984**, 81, 511–519.

42. Hoover, W. G. Canonical dynamics: equilibrium phase-space distribution. *Phys. Rev. A* **1985**, 31, 1695–1697.